Light Coupling and Trapping in Ultrathin Cu(In,Ga)Se_2 Solar Cells Using Dielectric Scattering Patterns

Claire van Lare,[†,§] Guanchao Yin,[‡,§] Albert Polman,[†] and Martina Schmid[*,‡,⊥]

[†]Center for Nanophotonics, FOM Institute AMOLF, Science Park 104, 1098 XG Amsterdam, The Netherlands, [‡]Nanooptische Konzepte für die Photovoltaik, Helmholtz-Zentrum Berlin für Materialien und Energie GmbH, Hahn-Meitner-Platz 1, 14109 Berlin, Germany, and [⊥]Department of Physics, Freie Universität Berlin, Arnimallee 14, 14195 Berlin, Germany. [§]C. van Lare and G. Yin contributed equally to this work.

ABSTRACT We experimentally demonstrate photocurrent enhancement in ultrathin Cu(In,Ga)Se_2 (CIGSe) solar cells with absorber layers of 460 nm by nanoscale dielectric light scattering patterns printed by substrate conformal imprint lithography. We show that patterning the front side of the device with TiO_2 nanoparticle arrays results in a small photocurrent enhancement in almost the entire 400−1200 nm spectral range due to enhanced light coupling into the cell. Three-dimensional finite-difference time-domain simulations are in good agreement with external quantum efficiency measurements. Patterning the Mo/CIGSe back interface using SiO_2 nanoparticles leads to strongly enhanced light trapping, increasing the efficiency from 11.1% for a flat to 12.3% for a patterned cell. Simulations show that optimizing the array geometry could further improve light trapping. Including nanoparticles at the Mo/CIGSe interface leads to substantially reduced parasitic absorption in the Mo back contact. Parasitic absorption in the back contact can be further reduced by fabricating CIGSe cells on top of a SiO_2-patterned In_2O_3:Sn (ITO) back contact. Simulations show that these semitransparent cells have similar spectrally averaged reflection and absorption in the CIGSe active layer as a Mo-based patterned cell, demonstrating that the absorption losses in the Mo can be partially turned into transmission through the semitransparent geometry.

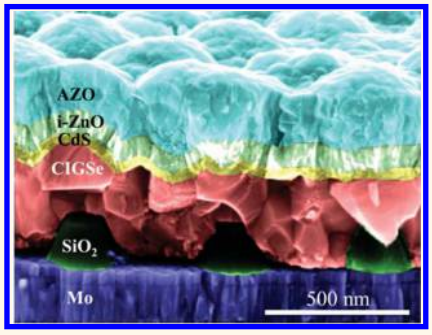

KEYWORDS: light trapping · chalcopyrite solar cells · dielectric scattering patterns · substrate conformal imprint lithography · J_{sc} enhancement

Cu(In,Ga)Se_2 (CIGSe) solar cells are promising thin-film candidates and have demonstrated efficiencies up to 21.7%.[1] One interesting aspect of CIGSe cells is that by varying the [Ga]/([Ga] + [In]) ratio the band gap can be varied between 1.0 and 1.7 eV,[2] which opens possibilities for tandem devices. Currently, the standard thickness for CIGSe absorbers is 2−3 μm, but in view of indium scarcity and to enhance cell-manufacturing throughput, it is favorable to reduce the thickness of the absorber layer. However, this poses two problems: First, thinning down the absorber layer thicknesses below 1 μm leads to strongly enhanced recombination at the back contact.[3] The recombination can be reduced by increasing the [Ga]/([Ga] + [In]) ratio toward the back contact ("back Ga grading"), leading to an effective electron reflector.[4] Second, reducing the active layer thickness below 1 μm leads to substantially reduced light absorption. Figure 1 shows the attenuation length of the CIGSe material used in this paper, which has a minimum band gap near 1200 nm (1.0 eV). The attenuation length was calculated ($l_{att} = \lambda/4\pi\kappa$, with λ the free space wavelength and κ the imaginary part of the refractive index) from the experimentally determined optical constants of the absorber material, which were extracted from reflection and transmission measurements on single layers deposited on glass.[5,6] This graph shows that reducing the absorber layer thickness to 1 μm leads to less than 1/e attenuation for all wavelengths above 1050 nm. Therefore, light trapping is required, in which nanostructures are used to scatter the incident light and thereby trap it in the absorber layer. The inset shows the general structure of a CIGSe solar cell, consisting of Mo, CIGSe, CdS, i-ZnO, and ZnO:Al (AZO).

Metal nanoparticles have gained much attention for light-trapping applications.[7−12] They exhibit plasmon resonances, which

* Address correspondence to martina.schmid@helmholtz-berlin.de.

Received for review December 22, 2014 and accepted September 8, 2015.

Published online 10.1021/acsnano.5b04091

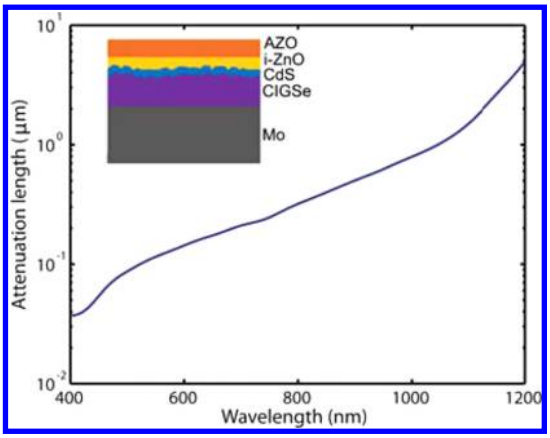

Figure 1. Measured 1/*e* attenuation length as a function of wavelength of CIGSe absorber material used in this work. The inset shows the general structure of a CIGSe solar cell geometry, consisting of Mo/CIGSe/CdS/i-ZnO/AZO.

leads to large scattering cross sections. However, these plasmonic light-trapping geometries also suffer from substantial absorption in the metal particles. Furthermore, metals are not thermally compatible with the growth process of the solar cells. Recently, dielectric nanoparticles have gained interest for light management in photovoltaic applications.[13−15] Wavelength-sized dielectric particles exhibit geometrical (Mie) resonances, with scattering cross sections comparable to those of metallic nanoparticles.[14−16] For a direct comparison of the scattering properties of dielectric and metallic nanoparticles see also ref 17. Dielectric materials with a relatively high refractive index and low absorption losses, such as TiO_2, AZO, and In_2O_3:Sn (ITO), can be used to pattern the front side of the device.[18] Alternatively, lower refractive index particles can be used at the rear side of the absorber layer, as long as they have sufficient index contrast with the absorber layer.[15,19]

Extensive research has been done on light trapping in thin-film Si and organic solar cells.[12,13,20−32] However, only a limited number of research groups have worked on light management in CIGSe cells,[3,33−36] and no experimental demonstration of light trapping in CIGSe cells has been published. Light trapping in ultrathin CIGSe cells is challenging because of the required stability of the light-trapping geometry during the high-temperature growth process, the difficulty of obtaining conformal growth of the absorber layer on the scattering pattern, and parasitic optical absorption in the Mo back contact. In fact, the absorption losses in the Mo back contact are a substantial loss factor in ultrathin CIGSe cells. Depositing the metal back contact on textured glass, which is often done to achieve light trapping in thin-film Si cells, is not an option, as it would lead to even higher absorption losses in the Mo. Replacing Mo with a different material remains challenging, due to the electronic quality of the contact and diffusion of the back contact material into the absorber layer. It was found that W, Nb, and Ta could replace Mo as a back contact material without affecting the growth of the absorber layer, but these materials still lead to much higher parasitic optical absorption than, for instance, Ag and Al.[37] CIGSe cells can also be grown on ITO or SnO_2:F (FTO) back contacts. Using transparent conductive oxides leads to substantially lower absorption in the back contact and is interesting for applications in multijunction devices. It was shown that a very thin $MoSe_2$ layer in between the ITO and the absorber layer, which facilitates carrier transport through tunneling, could lead to high-quality devices by making a quasi-ohmic contact.[38]

In this paper we use dielectric scattering patterns to enhance absorption in ultrathin CIGSe cells with an absorber layer thickness of only 460 nm. The particles are printed using substrate conformal imprint lithography (SCIL), in which a bilayer polydimethylsiloxane (PDMS) stamp is used to print nanostructures.[39] The stamp consists of a thick low Young's modulus PDMS layer, which allows printing over nonflat areas, such as metal grids, and of a thin high Young's modulus PDMS layer that holds the small nanostructures. The stamp is made from a Si master that is produced by electron beam (e-beam) lithography. SCIL allows for large-area fabrication of nanopatterns with a resolution determined by e-beam lithography. Promising results have been observed on roll-to-roll processes that focus on increasing throughput of this fabrication method.[40] We study the influence of dielectric scatterers both at the front of the device and at the interface between the absorber layer and the back contact. We found that both light incoupling and light trapping are enhanced by the nanoparticles. Finally, we study the effect of the light-trapping patterns on cells with ITO back contacts, paving the way for high-efficiency tandem architectures.

RESULTS

TiO_2 Surface Scattering Patterns. Figure 2a shows an SEM image of a cross section of an ultrathin CIGSe cell. Some roughness is observed at the CIGSe top interface, which also propagates in the CdS layer and flattens out in the top of the layers. Figure 2b shows the topography of the CIGSe layer, measured by atomic force microscopy (AFM) before the CdS/i-ZnO/AZO stack was deposited. Figure 3a shows current density−voltage (*JV*) measurements for flat cells before printing nanoparticles on top (black) and the same cells after printing periodic arrays of TiO_2 particles on top (red). The inset shows a schematic of the cell geometry, and the inset in Figure 3c shows an SEM image of the TiO_2 particle array printed onto the completed solar cells. The square array geometry has a pitch of 500 nm, particle radius of 120 nm, and particle height of 120 nm. *JV* measurements were done using a WACOM dual-beam solar simulator under 1 sun AM1.5 illumination. Data for the flat and patterned cells are averaged over four cells. A slight increase in J_{sc} is observed for the nanopatterned

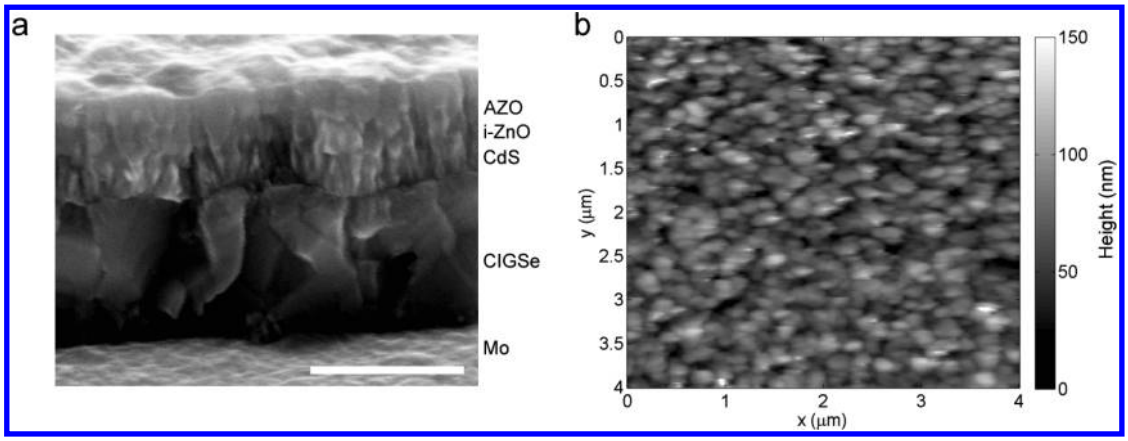

Figure 2. (a) SEM image of a cross section of an unpatterned CIGSe solar cell. The scale bar indicates 500 nm. (b) AFM scan of the surface topography of the CIGSe layer.

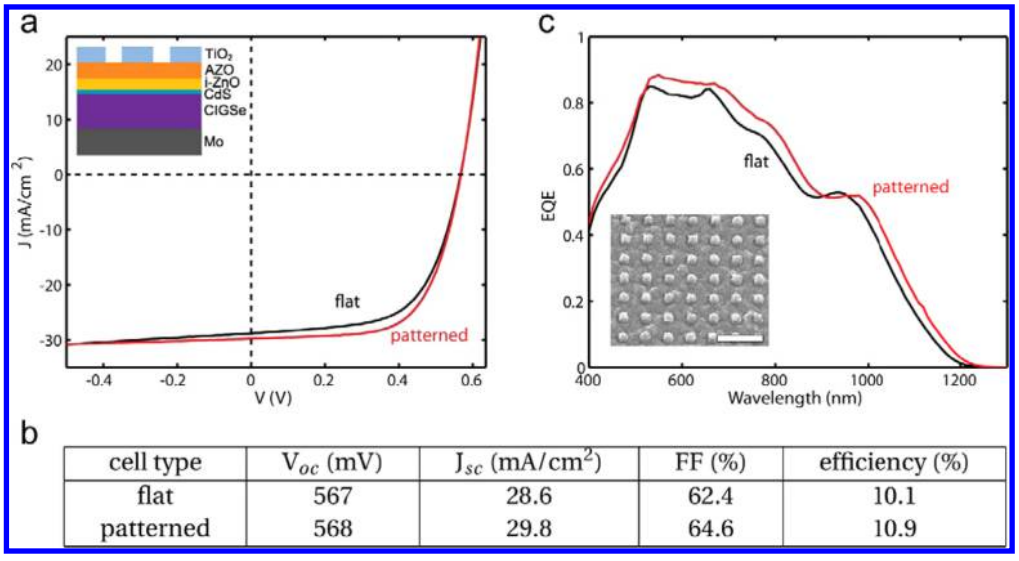

cell type	V_{oc} (mV)	J_{sc} (mA/cm^2)	FF (%)	efficiency (%)
flat	567	28.6	62.4	10.1
patterned	568	29.8	64.6	10.9

Figure 3. (a) *JV* measurements for flat cells (black) and cells with a periodic array of TiO_2 particles on top (red). The inset schematically shows the cell geometries for the patterned cells, consisting of a Mo/CIGSe/CdS/i-ZnO/AZO stack and TiO_2 nanoparticles. (b) Extracted parameters from the *JV* measurements. (c) EQE measurements for the flat (black) and patterned (red) cells in (a). The inset shows an SEM image of the patterned front surface. The scale bar indicates 1 μm.

cells. The higher slope at negative bias for the flat cells (black) indicates a lower parallel resistance for these cells. Figure 3b shows the electrical parameters extracted from the *JV* measurements. Differences in open-circuit voltage (V_{oc}) and fill factor (FF) are small between the different cell types. For both cell types V_{oc} and FF are relatively low, indicating a suboptimal quality of the active layers. Overall, the patterning does not significantly influence the electrical parameters of the cell, indicating that SCIL printing is very well compatible with CIGSe solar cells. This could be further confirmed by redoing the experiments with optimal-quality devices.

Figure 3c shows external quantum efficiency (EQE) spectra measured for flat (black) and patterned (red) cells. The EQE was measured with a two-source illumination system, consisting of a Xe and a halogen lamp with a 5 mm^2 spot size on the sample. The total light power in the spot was calibrated using certified Si and Ge reference diodes. The EQE for the flat cell (black) shows oscillations at wavelengths above 500 nm that we attribute to Fabry–Perot effects in the CdS/i-ZnO/AZO layer stack. Similarly, the main peak near 1000 nm is attributed to a Fabry–Perot interference in the CIGSe layer, since the absorption length exceeds the device thickness at that wavelength (see Figure 1). At wavelengths above 650 nm the EQE decreases rapidly due to poor absorption in the ultrathin CIGSe layer. Compared to the flat cell, the patterned cell (red) shows an enhanced EQE in the 500–1200 nm spectral range, with the exception of a narrow wavelength band from 900 to 950 nm.

Three-dimensional finite-difference time-domain (FDTD) simulations, performed using Lumerical FDTD software,[41] were used to study the optical performance of the devices in more detail. The complete thin-film stack was taken into account, and the topography of the CIGSe/CdS interface as measured using AFM (Figure 2b) was included by directly importing the AFM data in the simulations. The topography of the

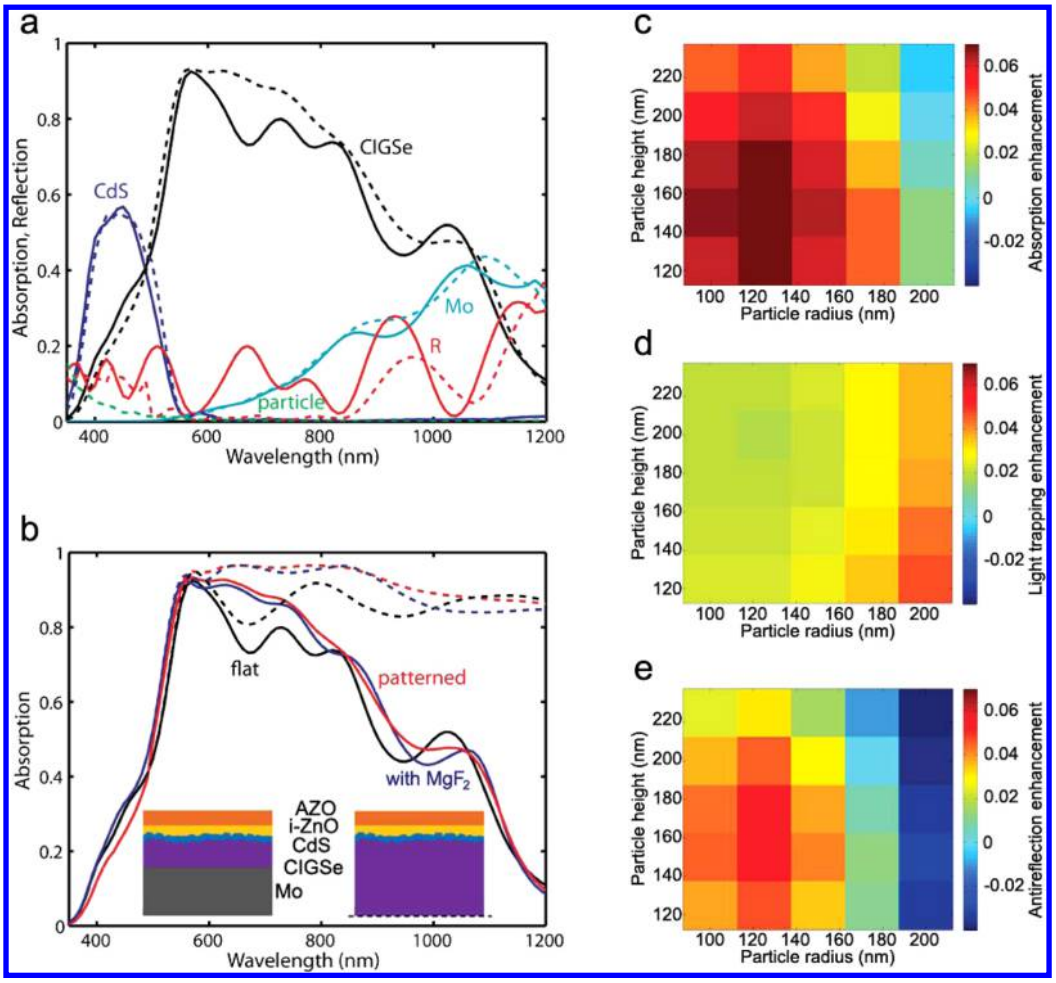

Figure 4. (a) Simulated absorption in Mo (cyan), CIGSe (black), CdS (blue), and TiO_2 particles (green) and simulated reflection (red) for cells with TiO_2 particles (dashed) and flat cells (continuous). (b) Simulated absorption in the CIGSe layer for flat (black), flat with a 110 nm MgF_2 layer (blue), and patterned (red) thin cells (continuous lines) and infinitely thick cells (dashed lines). The insets show the cell geometries for the thin cell (left) and the infinitely thick cell (right). The dashed line indicates the bottom PML boundary used in the simulation. (c) AM1.5 averaged absorption enhancement in patterned cells with different combinations of particle radius and height and an array pitch of 450 nm. (d) AM1.5 averaged light-trapping enhancement for the same array geometries as in (c). (e) AM1.5 averaged antireflection enhancement for the same geometries as in (c) and (d).

CdS/i-ZnO interface was assumed to be identical to that at the CIGSe/CdS interface with the height variations halved. The optical constants of all layers except for the Mo layer were extracted from transmission and reflection measurements on single layers on glass substrates as described in refs 5 and 6. Optical constants of the Mo layer were determined by ellipsometry. Optical constants of the TiO_2 layer were determined by spectroscopic ellipsometry on a flat TiO_2 layer, deposited using the same evaporation parameters as for the nanoparticles. A uniform 5 nm mesh was used over the entire simulation volume; this mesh size was chosen after mesh convergence testing. Perfectly matched layers were used at the top and bottom of the simulation volume, and periodic boundary conditions were used in *x* and *y* dimensions. Varying the box size of a cell without nanoparticles between 400 nm and 1 μm did not show significant differences in the simulated absorption, indicating that discontinuities at the boundaries, caused by the roughness at the CIGS/CdS interface, do not significantly influence the results. Figure 4a shows the FDTD-simulated reflection and absorption spectra for the different layers of the device for flat cells (continuous lines) and patterned cells (dashed lines). The FDTD simulations create the possibility to study the absorption in all layers of the device stack separately, which would not be possible experimentally. The absorption spectrum for the flat cell shows Fabry–Perot oscillations at wavelengths above 500 nm. Compared to the EQE measurements in Figure 3c, these oscillations are somewhat more pronounced, which we attribute to differences in roughness of the device between the experiment and the simulation and to the fact that the simulation assumes full collection of carriers generated in the active CIGSe layer, while in reality this may not be the case. Furthermore, compared to the experiment, the oscillations are slightly red-shifted in the simulation, which we attribute to differences in the layer thickness between the experiment and the simulation. In particular the CdS layer,

which is deposited in a chemical bath, is susceptible to thickness deviations. In the simulations we set the thickness of the CdS layer to 50 nm, which was the desired thickness for this layer in the experiment. Similar to the trend in the EQE measurements, the patterned cell (red) shows an enhanced response over almost the entire wavelength range. Overall, the simulated absorption data agree well with the trends in the experimentally determined EQE data.

Figure 4a also shows that absorption in the TiO_2 nanoparticles, averaged over the AM1.5 spectrum, is below 1%. Supplementary Figure S1 shows the experimentally determined optical constants for the TiO_2, demonstrating the low imaginary part of the refractive index. Absorption in the Mo back contact (cyan) is large at wavelengths where the device is not optically thick (>800 nm). This poses a main limitation in the efficiency of ultrathin CIGSe cells. Patterning the cell at the front side leads to a small increase in the absorption in the Mo layer. Absorption in the CdS (blue) is a significant loss factor at wavelength up to 550 nm and remains almost unchanged upon patterning the cell. Absorption in the AZO and i-ZnO layers is relatively low and does not change significantly upon patterning the cell (not shown). The simulated absorption spectra show that patterning the cell at the front mostly enhances the absorption in the CIGSe layer at wavelengths between 450 and 950 nm, whereas the enhancement is small at larger wavelengths, where absorption in the CIGSe layer is weaker. To distinguish between light trapping and antireflection effects of the nanoparticles, Figure 4b compares the simulated absorption in thin cells (continuous lines) to cells with an infinitely thick absorber layer (dashed lines). At wavelengths up to 570 nm, the absorption spectra for thin and thick flat cells are similar; the same is observed when comparing thin and thick patterned cells. At these wavelengths the CIGSe layer is still optically thick. At larger wavelengths, the absorption in the thin cells starts to deviate from the absorption in the thick cells. Both the thick and the thin flat cells show a dip at 700 nm, which is attributed to a Fabry–Perot effect in the window layers, and in both cases patterning the cells leads to a similar absorption enhancement. We note that while the comparison in Figure 4 is made against a flat cell, in reality the unpatterned geometry has surface and interface roughness, as can be seen in Figure 2. Supplementary Figure S2 compares the absorption in CIGSe and CdS in a flat layer stack and in a layer geometry with roughness as in the SEM cross section in Figure 2. Interface roughness leads to reduced absorption in the CIGSe layer in the blue spectral range, which is caused by additional absorption in the CdS layer. The absorption in the CIGSe in the red spectral range shows the same overall trend for the two geometries.

Overall, comparing results for thick and thin cells shows that the enhancement obtained by patterning a thick cell on the front is very similar to the enhancement obtained when patterning a thin cell. Since the enhanced absorption in an infinetly thick cell can only be due to an antireflection effect, this indicates that patterning mostly results in an antireflection effect and that light trapping does not significantly contribute to the enhanced absorption in thin patterned cells. This antireflection effect is due to preferential forward scattering of the light by the nanoparticles, since the TCO layers below have a larger refractive index than air, as demonstrated earlier for among others Si wafers and thin-film amorphous Si solar cells.[11,14,17,42] For reference, in Figure 4b we show the simulated absorption for an optimized antireflection coating of 110 nm MgF_2 for thin (continuous) and infinitely thick (dashed) cells; the performance of these cells is comparable to the cells with dielectric front patterns.

FDTD simulations were used to optimize the array geometry for maximum AM1.5 averaged absorption enhancement in the CIGSe layer, defined by

$$\frac{\int_{\lambda_{min}}^{\lambda_{max}} A_{p,\,thin}\mathrm{AM1.5}d\lambda - \int_{\lambda_{min}}^{\lambda_{max}} A_{f,\,thin}\mathrm{AM1.5}d\lambda}{\int_{\lambda_{min}}^{\lambda_{max}} A_{f,\,thin}\mathrm{AM1.5}d\lambda}$$

with AM1.5 being the photon flux in the AM1.5 spectrum, $A_{p,thin}$ and $A_{f,thin}$ being the absorption in the patterned and the flat thin cell, respectively, λ_{min} = 350 nm, and λ_{max} = 1200 nm. To find the best geometry, a parameter sweep was done over the particle radius, height, and the array pitch, using a square array geometry. Figure 4c shows the calculated absorption enhancement as a function of particle radius and height for an array pitch of 450 nm. It shows that the geometry with a particle radius of 125 nm and height of 150 nm results in the largest absorption enhancement. To study the contribution of light trapping for different array geometries, we compare the difference in enhancement between patterning a thin cell and patterning an infinitely thick cell with the same array geometry. Figure 4d shows the light-trapping enhancement, defined by

$$\frac{\left[\int_{\lambda_{min}}^{\lambda_{max}} A_{p,\,thin}\mathrm{AM1.5}d\lambda - \int_{\lambda_{min}}^{\lambda_{max}} A_{f,\,thin}\mathrm{AM1.5}d\lambda\right] - \left[\int_{\lambda_{min}}^{\lambda_{max}} A_{p,\,thick}\mathrm{AM1.5}d\lambda - \int_{\lambda_{min}}^{\lambda_{max}} A_{f,\,thick}\mathrm{AM1.5}d\lambda\right]}{\int_{\lambda_{min}}^{\lambda_{max}} A_{f,\,thin}\mathrm{AM1.5}d\lambda}$$

where $A_{p,thick}$ is the absorption in a thick patterned cell and $A_{f,thick}$ is the absorption in a thick flat cell. Whereas the geometry with radius 125 nm and height 150 nm results in the largest overall absorption enhancement,

shown in Figure 4c, the contribution of light trapping is small for this array geometry. The light trapping increases for larger particle radii, but increasing the radius comes at the expense of the total absorption enhancement.

Figure 4e shows the antireflection enhancement, defined by

$$\frac{\int_{\lambda_{min}}^{\lambda_{max}} A_{p,\,thick}\mathrm{AM1.5}d\lambda - \int_{\lambda_{min}}^{\lambda_{max}} A_{f,\,thick}\mathrm{AM1.5}d\lambda}{\int_{\lambda_{min}}^{\lambda_{max}} A_{f,\,thin}\mathrm{AM1.5}d\lambda}$$

which can be accessed *via* the enhancement upon patterning an infinitely thick cell, but for comparison we normalized to the absorption of a thin flat cell. The trends observed in the antireflection enhancement for different array geometries are very similar to the trends in the total absorption enhancement in Figure 4c, demonstrating that the absorption enhancement in a thin cell mostly relies on the antireflection effect caused by the nanoparticles. The use of particles with a large radius, which results in increased light trapping, but decreased total absorption enhancement, causes the antireflection enhancement to be negative, indicating that transmission into the solar cell decreases upon patterning. Overall, Figure 4c–e show that maximizing the absorption enhancement of the patterned thin-film geometry relies on optimizing the antireflection properties of the scattering pattern. We find the same trend as in Figure 4c–e for different array pitches in the range 400–650 nm.

SiO_2 Backscattering Patterns. To achieve light trapping in ultrathin CIGSe cells, we fabricated arrays of SiO_2 nanoparticles at the Mo/CIGSe interface. Figure 5a shows an SEM image of a cross section of the device that was made by breaking the cell after scribing the glass. The particle array is visible as an array of dark hemispheres on top of the Mo layer. The CIGSe layer was deposited on top of the particle array and conformally fills the gaps in between the particles, enabling good electrical contact. In the subsequent layer deposition the pattern caused by the particle array flattens out, but significant corrugation is still observed at the front side of the device.

Figure 5b shows the *JV* measurements for flat cells (back) and patterned cells (red). Both cell types were produced in the same deposition batch; similar cells from the same batch show very reproducible J_{sc}. Data are averages of six cells. The patterned and unpatterned cells show similar overall shapes of the *JV* curves, while the patterned cells show a clear enhancement in J_{sc}. Figure 5c summarizes the electrical parameters for the different cell types. Patterning of the cells leads to an enhancement in V_{oc} from 583 mV to 592 mV and in J_{sc} from 28.6 mA/cm^2 to 30.6 mA/cm^2, the latter being directly the result of the enhanced absorption of the incident light. A slight enhancement in FF from 67.4% to 68.2% is obtained upon patterning the cells. Overall these data show that growing cells on top of SCIL-printed SiO_2 particles on Mo does not significantly deteriorate the electrical properties of the device; a small increase is even observed in FF and V_{oc}. A slight enhancement in V_{oc} is due to the enhancement in J_{sc}, as given by $V_{oc} = (nk_BT/q)\ln[J_{sc}/(J_0 + 1)]$, where n is the diode ideality factor, k_B is the Boltzmann constant, T is the temperature, q is the charge of an electron, and J_0 is the dark saturation current. Furthermore, the presence of the SiO_2 particles could result in a reduction in minority carrier recombination, by reducing the interfacial area between the Mo back contact and the CIGSe absorber layer. This effect was also seen in ref 43, which used a thin Al_2O_3 layer at the CIGSe/Mo interface with holes in order to form point contacts. Further experiments would be required to study this. It can be noted that the flat cells presented in Figure 5 show higher efficiencies than the flat cells in Figure 3, which is due to the fact that they were produced in different batches. These differences are due to different V_{oc} and FF values. The photocurrent, which is the parameter that will be mostly affected by light trapping, is equal for the flat cells from the two different deposition batches. The SiO_2 in the light-trapping pattern has the advantage of being a thermally stable material. The cells used in this paper were grown at a lower temperature than the record CIGSe cell. A study of the thermal stability of geometries containing this SiO_2 pattern grown at higher temperature is beyond the scope of this paper. However, high-efficiency CIGSe cells can also be grown at low temperatures.[44] Low-temperature deposition is even a research trend because it allows for cell depositions on flexible substrates.

In addition, low-temperature deposition can facilitate a high back Ga grading, which is important to reduce back recombination in ultrathin cells. We also made well-performing devices with SiO_2 back patterns at a deposition temperature above 500 °C; they did not show deterioration of electrical properties with respect to their flat counterparts. However, the photocurrent enhancement we found for these patterned devices was not as obvious as in Figure 5 due to high back recombination, due to the absence of a strong Ga grading.

Figure 5d shows the EQE measurements for flat (black) and patterned (red) cells. For wavelengths up to 550 nm the flat and patterned cells show a similar response, indicating that the corrugation at the front side of the devices, which is caused by conformal growth on the particle arrays, does not significantly influence the incoupling of the incident light. For wavelengths above 700 nm the EQE of the flat cells (black) decreases significantly due to incomplete absorption of the incident light in the ultrathin-absorber

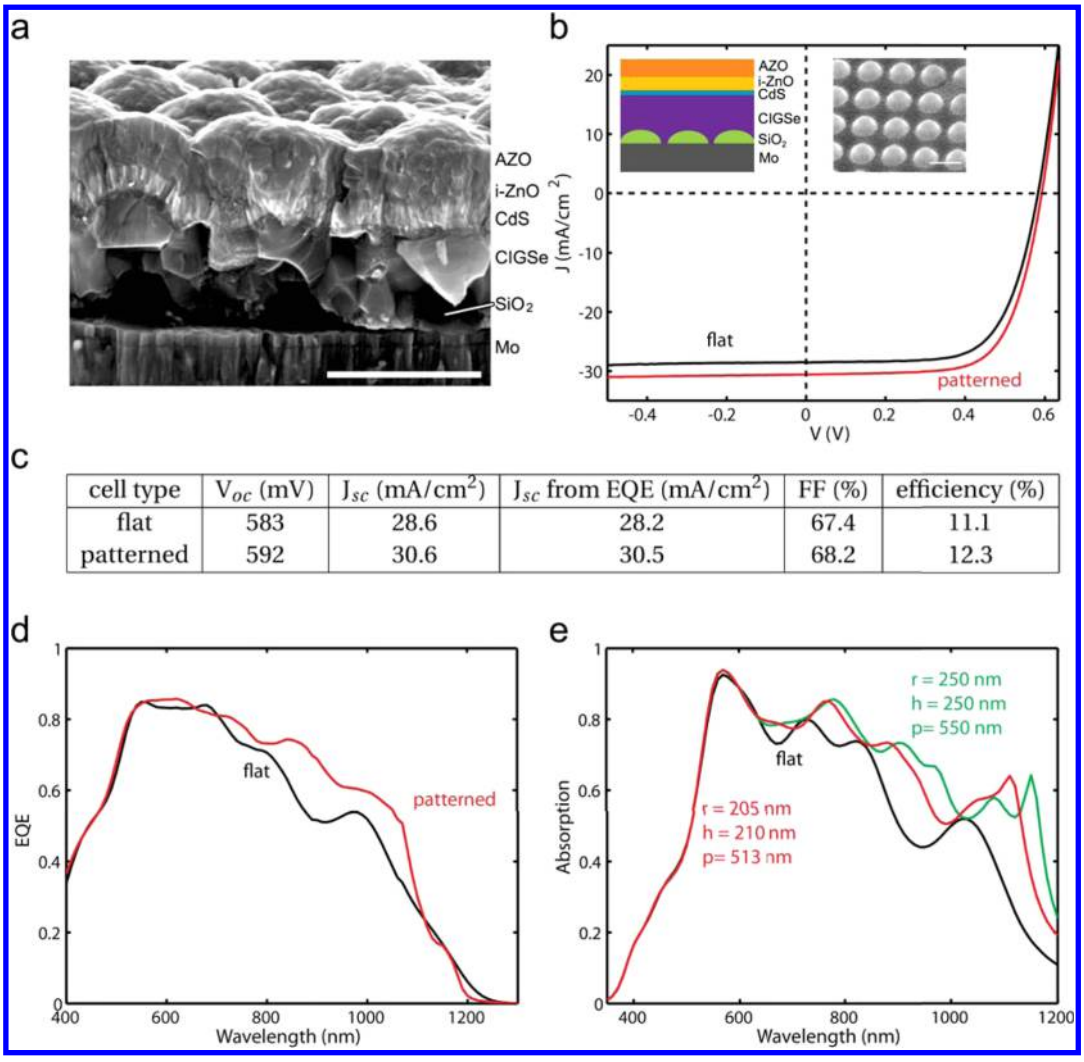

cell type	V_{oc} (mV)	J_{sc} (mA/cm^2)	J_{sc} from EQE (mA/cm^2)	FF (%)	efficiency (%)
flat	583	28.6	28.2	67.4	11.1
patterned	592	30.6	30.5	68.2	12.3

Figure 5. (a) SEM image of a cross section of a CIGSe solar cell with a periodic array of nanoparticles at the Mo/CIGSe interface. The scale bar indicates 500 nm. (b) *JV* measurements for flat (black) CIGSe cells and cells with arrays of SCIL-printed SiO_2 particles at the CIGSe/Mo interface (red). The insets show a schematic cross section of the patterned cell (left) and an SEM image of the SiO_2-patterned Mo layer (right). The scale bar indicates 500 nm. (c) Summary of the electrical parameters for both cell types. (d) EQE measurements on the same cell types. (e) FDTD-simulated absorption for a flat cell (black), cell with the same nanopattern as in the experiment (red), and cell with an optimized nanopattern (green).

layer. The patterned cells (red) show a substantial enhancement in this spectral range due to light trapping. To exclude the effect of inaccuracies in the determination of the surface area of these small cells (0.5 cm^2) on the determination of J_{sc}, J_{sc} was also calculated from the EQE measurements (Figure 5c), and these values were used to calculate the cell efficiencies. Overall, patterning the back contact of the cell results in a significant increase in efficiency from 11.1% to 12.3%, calculated with the corrected J_{sc} values. It should be noted that these efficiencies are well below the CIGSe record efficiency (efficiency, 21.7%; V_{oc}, 746 mV; J_{sc}, 36.6 mA/cm^2; FF, 79.3%).[45] The CIGSe record cell is significantly thicker and the device is fully optimized, whereas in this paper the emphasis is on demonstrating the light-trapping concept. The differences in performance between the ultrathin cells presented here and the record cell are mostly in V_{oc} and FF. This gap is attributed to both bulk and interface recombination, which can be reduced by optimizing the deposition process, introducing KF treatment on the CIGSe absorber,[44] and using a point-contact structure at the CIGSe/back contact.[43] Optimization of V_{oc} and FF is beyond the scope of work in this contribution. J_{sc} is typically below 30 mA/cm^2 for bare ultrathin CIGSe solar cells;[3,4] we demonstrated a value beyond 30 mA/cm^2 using the dielectric back pattern. An additional gain in J_{sc} of around 2 mA/cm^2 can be expected after coating the cell with a MgF_2 antireflection layer,[46] which was also applied in the record cell. This substantially reduces the gap in J_{sc}. Further enhancement in absorption or J_{sc} can be achieved by replacing the Mo layer by a less absorbing back reflector and by replacing CdS by a high-band-gap buffer layer, such as Zn(O,S).[47]

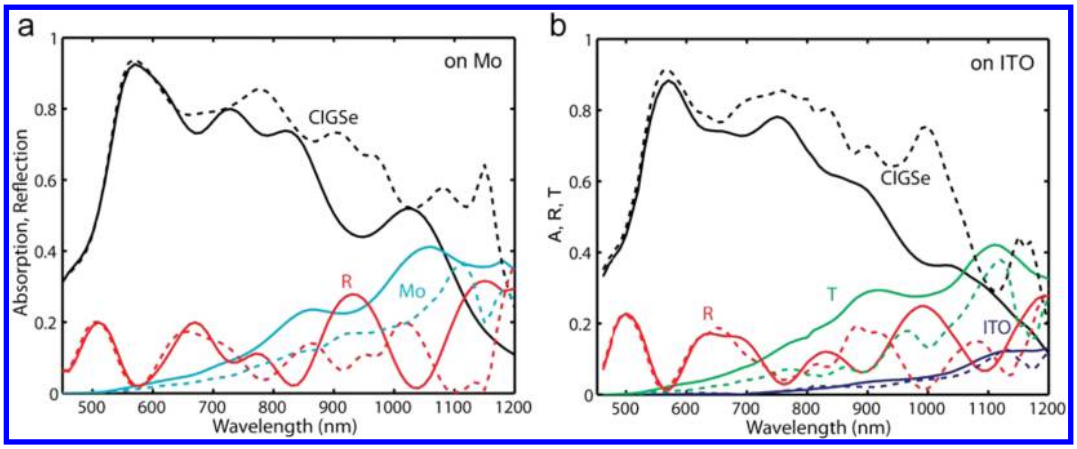

Figure 6. Simulated optical losses in thin-film CIGSe cells on (a) Mo and (b) ITO back contact. Data are shown for flat cells (continuous lines) and patterned cells (dashed lines). Simulated absorption is shown in the CIGSe layer (black), Mo layer (cyan), ITO layer (blue); simulated reflection is also shown (red). In (b) the simulated transmission through the device stack (green) is shown.

It is interesting to reflect on the mechanical and thermal stability of the nanoimprinted cell geometry. For the top-contacted geometries, the TiO_2 particles are evaporated onto the cells, and it is known that such evaporation leads to good adherence to the surface. The embedded SiO_2 particles are conformally coated with the subsequently deposited layers, without voids, and are thus in a mechanically robust environment. SiO_2 (glass temperature above 1000 °C) and TiO_2 (melting point 1843 °C) are known for high thermal stability and will easily survive at the CIGSe growth temperatures beyond 500 °C. We note further that the cells used in our paper were grown at a lower temperature (440 °C) than the record CIGSe cell. High-efficiency CIGSe cells can also be grown at low temperatures.[44] Futhermore, low-temperature deposition can facilitate a high back Ga grading, which is important to reduce back recombination in ultrathin cells. A detailed experimental study on the thermal stability of light-trapping patterns in cells grown at high temperature is beyond the scope of this paper.

To study the back-pattern geometry in more detail, FDTD simulations were performed. In the simulations, the absorber layer thickness of the patterned cell was increased to compensate for the volume excluded by the SiO_2 particles, so that the total absorber volume was the same for the flat and patterned geometries. Optical constants for the SiO_2 particles were taken from the literature.[48] Figure 5e shows the simulated absorption in the CIGSe layer for flat (black) and patterned (red) cells. The trends in simulated absorption are in good agreement with the trends in EQE measurements. Up to 650 nm, the absorption spectra for flat and patterned cells are similar. At larger wavelengths the patterned cell shows significantly enhanced absorption. A clear absorption peak is observed near 1100 nm, which is also rudimentarily present in the EQE measurements in Figure 5d. In additional simulations, keeping particle height and diameter constant and increasing the array pitch, we find the peak wavelength increases with the array pitch. We attribute this peak to waveguide-mode coupling.[15,42] Finally, we optimized the array geometry by changing the particle radius and height and found a further optimized absorption spectrum for the CIGSe layer (Figure 5d, green). The optimum geometry has particles with radius 250 nm, height 250 nm, and an array pitch of 550 nm.

Figure 6a shows the simulated absorption in all different layers as well as the reflection for the flat (continuous lines) and optimized patterned (dashed lines) cells. At wavelengths for which cell patterning leads to enhanced absorption in the CIGSe layer (black), also a changed reflection spectrum is observed. Overall the patterning leads to a reduced reflection. Furthermore, patterning also leads to a substantial reduction of absorption in the Mo back contact (cyan). Absorption in the AZO, i-ZnO, and CdS layers does not significantly change upon patterning the Mo/CIGSe interface of the device (not shown).

Since absorption in the Mo back contact is a major loss factor in thin-film CIGSe cells, growth of absorber layers on alternative back contacts is of great interest. Figure 6b shows the simulated reflection, transmission, and absorption in SiO_2 patterned (dashed lines) and unpatterned (continuous lines) devices on ITO back contacts with a thickness of 200 nm. Whereas the cells on Mo showed up to 40% absorption in the back contact (for the flat cell, at 1050 nm), the absorption in the ITO layer of this geometry is always below 15%. The absorption in the flat CIGSe cell on ITO (black, continuous line) rapidly decreases at wavelengths above 750 nm. Compared to the geometry with Mo in Figure 6a the overall absorption in the CIGSe layer is lower. The average reflection from the flat cell on ITO is similar to the reflection for the cell on Mo.

The layer stack shows increasing transmission at wavelengths above 550 nm, exceeding 40% at 1120 nm.

However, patterning the ITO layer with SiO_2 particles leads to a substantially enhanced absorption in the CIGSe layer (black, dashed line) over the entire 600−1200 nm spectral range. This absorption enhancement is mainly due to reduced transmission (green). Patterning also leads to a slight reduction in the reflection (red) and in the absorption in the ITO layer (blue). For this optimized patterned ITO geometry, the AM1.5-spectrum-averaged absorption is the same as for the patterned cell on Mo (61%). At the same time, the main losses in this optimized ITO geometry are due to reflection, which is similar to that for a patterned Mo cell (11% averaged over the AM1.5 spectrum), and transmission rather than parasitic absorption, as is the case for the Mo cells. This is an important result and makes the ITO-based patterned ultrathin CIGSe cells interesting candidates for semitransparent devices. Furthermore, in combination with a flat Ag back reflector, which can simply be deposited at the rear side of the glass substrate, the cell absorption in the CIGSe layer could be further improved. In tandem geometries that consist of wide-band-gap chalcopyrite top cells (such as $CuGaSe_2$ with E_g = 1.7 eV) on narrow-band-gap bottom cells (such as $Cu(In,Ga)Se_2$ with low Ga content, E_g = 1.1 eV), the low subgap transparency of the top chalcopyrite absorber has been identified as a bottleneck.[49,50] A back-patterned ultrathin wide-gap chalcopyrite absorber is an interesting candidate to overcome these limitations, since it combines light absorption enhancement above the band gap with high subgap transparency.

CONCLUSION

We have fabricated dielectric scattering patterns on the front and back side of ultrathin CIGSe solar cells with absorber layer thicknesses of 460 nm. We showed that printing arrays of TiO_2 nanoparticles at the front side of completed CIGSe solar cells results in a photocurrent enhancement in the 550−950 nm spectral range, which is mostly due to an antireflection effect caused by preferential forward scattering of light. Exploring different array geometries showed that the array geometry of TiO_2 particles on the front side can be optimized for light trapping, but this comes at the expense of the total absorption enhancement. We demonstrated that efficient light trapping can be achieved in these cells by using arrays of SiO_2 particles at the Mo/CIGSe interface. This leads to efficient light trapping and does not deteriorate, and maybe even improves, the carrier recombination properties of the device, resulting in a significant cell efficiency increase from 11.1% to 12.3%. Whereas the dielectric scatterers lead to a substantial reduction of the absorption in the Mo back contact, absorption in this layer is still a significant loss factor. This can be avoided in a semitransparent geometry in which cells are grown on SiO_2 nanopatterned ITO, turning the absorption loss in the Mo layer into absorption loss in the ITO layer and transmission.

METHODS

CIGSe absorber layers ([Ga]/([Ga] + [In]) = 0.36, [Cu]/([Ga] + [In]) = 0.86) with a thickness of only 460 nm were deposited by a three-stage coevaporation process[51,52] on Mo-coated soda-lime glass substrates at a relatively low substrate temperature of 440 °C. The low-temperature deposition enabled preservation of the intentional deposition sequence of Ga−Se prior to In−Se in the first stage and thus facilitated the formation of a higher back [Ga]/([Ga] + [In]) grading and reduced back recombination.[4] Subsequently a 50 nm CdS buffer layer was grown *via* chemical bath deposition in a solution with 1.1 M ammonia, 0.14 M thiourea, and 0.002 M cadmium acetate. This was followed by magnetron sputtering of 130 nm i-ZnO and 240 nm AZO. The solar cells were mechanically scribed to divide the cells into 0.5 cm^2 areas, exactly according to metal scales on the cells, which are deposited through a mask by e-beam evaporation. This results in a high accuracy of the cell area and leads to comparable cell areas for different cells. All cells were scribed using this same procedure, so that J_{sc} values can be compared within 2%. Metal grids, consisting of 10 nm thick Ni and 1 μm thick Al, were evaporated on top. Substrate conformal imprint lithography was used to fabricate dielectric particles at the back and front side of the device. To pattern the front side, the sample was first spin-coated with a 550 nm PMMA layer and then with a 70 nm sol−gel layer, and the sol−gel layer was then patterned with an array of holes using SCIL.[39] Reactive ion etching was used to break through the remaining sol−gel layer underneath the holes and subsequently to transfer the holes to the PMMA layer. This was followed by e-beam evaporation of TiO_2. Lift-off of the mask was performed by dissolving the PMMA mask in a 50 °C acetone solution. To pattern the back side, SCIL was used to pattern a sol−gel layer on top of PMMA on the Mo-coated substrate followed by reactive-ion etching, e-beam evaporation of SiO_2, and lift-off of the mask. The Mo layer with dielectric nanoparticles was then used as a substrate for deposition of the subsequent device layers.

Conflict of Interest: The authors declare no competing financial interest.

Acknowledgment. The authors would like to thank C. Kelch, M. Kirsch, and J. Albert for technical support. SARA Computing and Networking Services is acknowledged for support in using the Lisa Computer Cluster. The authors acknowledge the funding from the Helmholtz-Association for Young Investigator groups within the Initiative and Networking fund (VH-NG-928). This work is also part of the research program of FOM, which is financially supported by NWO. Additionally, it is funded by the European Research Council, the Global Climate and Energy Project (GCEP), and NanoNextNL, a technology program of the Dutch Ministry of Economy Affairs. G.Y. specially acknowledges the support of funding from China Scholarship Council.

Supporting Information Available: The Supporting Information is available free of charge on the ACS Publications website at DOI: 10.1021/acsnano.5b04091.

Additional figures (PDF)

REFERENCES AND NOTES

1. New Best Mark in Thin-Film Solar Performance with 21.7% Efficiency. http://www.zsw-bw.de/en/support/press-releases/press-detail/zsw-brings-world-record-back-to-stuttgart.html, 2014.
2. Wei, S.; Zunger, A. Band Offsets and Optical Bowings of Chalcopyrites and Zn-Based II-VI Alloys. *J. Appl. Phys.* **1995**, *78*, 3846–3856.

3. Gloeckler, M.; Sites, J. R. Potential of Submicrometer Thickness Cu(In,Ga)Se_2 Solar Cells. *J. Appl. Phys.* **2005**, *98*, 103703.
4. Yin, G.; Brackmann, V.; Hoffmann, V.; Schmid, M. Enhanced Performance of Ultra-Thin Cu(In,Ga)Se_2 Solar Cells Deposited at Low Process Temperature. *Sol. Energy Mater. Sol. Cells* **2015**, *132*, 142–147.
5. Yin, G.; Merschjann, C.; Schmid, M. The Effect Of Surface Roughness on the Determination of Optical Constants of $CuInSe_2$ and $CuGaSe_2$ Thin Films. *J. Appl. Phys.* **2013**, *113*, 213510.
6. Yin, G.; Manley, P.; Schmid, M. Influence of Substrate and its Temperature on the Optical Constants of $CuIn_{1-x}Ga_xSe_2$ Thin Films. *J. Phys. D: Appl. Phys.* **2014**, *47*, 135101.
7. Haug, F.-J.; Söderström, T.; Cubero, O.; Terrazzoni-Daudrix, V.; Ballif, C. Plasmonic Absorption in Textured Silver Back Reflectors of Thin Film Solar Cells. *J. Appl. Phys.* **2008**, *104*, 064509.
8. Diukman, I.; Orenstein, M. How Front Side Plasmonic Nanostructures Enhance Solar Cell Efficiency. *Sol. Energy Mater. Sol. Cells* **2011**, *95*, 2628.
9. Bhattacharya, J.; Chakravarty, N.; Pattnaik, S.; Slafer, W. D.; Biswas, R.; Dalal, V. L. A Photonic-Plasmonic Structure for Enhancing Light Absorption in Thin Film Solar Cells. *Appl. Phys. Lett.* **2011**, *99*, 131114.
10. Catchpole, K. R.; Polman, A. Plasmonic Solar Cells. *Opt. Express* **2008**, *16*, 21793.
11. Atwater, H. A.; Polman, A. Plasmonics for Improved Photovoltaic Devices. *Nat. Mater.* **2010**, *9*, 205–213.
12. Li, X.; Choy, W.; Huo, L.; Xie, F.; Sha, W.; Ding, B.; Guo, X.; Li, Y.; Hou, J.; You, J.; *et al*. Dual Plasmonic Nanostructures for High Performance Inverted Organic Solar Cells. *Adv. Mater.* **2012**, *24*, 3046–3052.
13. Basch, A.; Beck, F. J.; Söderström, T.; Varlamov, S.; Catchpole, K. R. Combined Plasmonic and Dielectric Rear Reflectors for Enhanced Photocurrent in Solar Cells. *Appl. Phys. Lett.* **2012**, *100*, 243903.
14. Spinelli, P.; Verschuuren, M. A.; Polman, A. Broadband Omnidirectional Antireflection Coating based on Subwavelength Surface Mie Resonators. *Nat. Commun.* **2012**, *3*, 692.
15. van Lare, M.; Lenzmann, F.; Polman, A. Dielectric Back Scattering Patterns for Light Trapping in Thin-Film Si Solar Cells. *Opt. Express* **2013**, *21*, 20738.
16. Bohren, C. F.; Huffman, D. R. *Absorption and Scattering of Light by Small Particles*; Wiley: New York, 2008.
17. Schmid, M.; Andrae, P.; Manley, P. Plasmonic and Photonic Scattering and Near Fields of Nanoparticles. *Nanoscale Res. Lett.* **2014**, *9*, 50.
18. Spinelli, P.; Macco, B.; Verschuuren, M.; Kessels, W.; Polman, A. Al_2O_3/TiO_2 Nano-Pattern Antireflection Coating with Ultralow Surface Recombination. *Appl. Phys. Lett.* **2013**, *102*, 233902.
19. van Lare, M.; Lenzmann, F.; Verschuuren, M.; Polman, A. Dielectric Scattering Patterns for Efficient Light Trapping in Thin-Film Solar Cells. *Nano Lett.* **2015**, *15*, 4846.
20. Zhu, J.; Hsu, C.-M.; Yu, Z.; Fan, S.; Cui, Y. Nanodome Solar Cells with Efficient Light Management and Self-Cleaning. *Nano Lett.* **2010**, *10*, 1979–1984.
21. Battaglia, C.; Escarré, J.; Söderström, K.; Charrière, M.; Despeisse, M.; Haug, F. J.; Ballif, C. Nanomoulding of Transparent Zinc Oxide Electrodes for Efficient Light Trapping in Solar Cells. *Nat. Photonics* **2011**, *5*, 535–538.
22. Pala, R. A.; Liu, J. S. Q.; Barnard, E. S.; Askarov, D.; Garnett, E. C.; Fan, S.; Brongersma, M. L. Optimization of Non-Periodic Plasmonic Light-Trapping Layers for Thin-Film Solar Cells *Nat. Commun.* **2013**, *4*, 10.1038/ncomms3095.
23. Soldera, M.; Estrada, E.; Taretto, K. Geometric Light Trapping in 2D and 3D Structured Small Molecule Organic Solar Cells. MRS Fall Meeting, **2012**.
24. Yu, K. J.; Gao, L.; Park, J. S.; Lee, Y. R.; Corcoran, C. J.; Nuzzo, R. G.; Chanda, D.; Rogers, J. A. Light Trapping: Light Trapping in Ultrathin Monocrystalline Silicon Solar Cells. *Adv. Energy Mater.* **2013**, *3*, 1528.
25. Battaglia, C.; Söderström, K.; Escarré, J.; Haug, F.-J.; Domine, D.; Cuony, P.; Boccard, M.; Bugnon, G.; Denizot, C.; Despeisse, M.; *et al*. Efficient Light Management Scheme for Thin Film Silicon Solar Cells *via* Transparent Random Nanostructures Fabricated by Nanoimprinting. *Appl. Phys. Lett.* **2010**, *96*, 213504.
26. Isabella, O.; Campa, A.; Heijna, M. C. R.; Soppe, W.; Erven, R. V.; Franken, R. H.; Borg, H.; Zeman, M. Diffraction Gratings for Light Trapping in Thin-Film Silicon Solar Cells. Proceedings of the 23rd European Photovoltaic Solar Energy Conference. Valencia, Spain, **2008**; pp 2320−2324.
27. Tan, H.; Santbergen, R.; Smets, A. H. M.; Zeman, M. Plasmonic Light Trapping in Thin-film Silicon Solar Cells with Improved Self-Assembled Silver Nanoparticles. *Nano Lett.* **2012**, *12*, 4070–4076.
28. Rockstuhl, C.; Fahr, S.; Bittkau, K.; Beckers, T.; Carius, R.; Haug, F.-J.; Söderström, T.; Ballif, C.; Lederer, F. Comparison and Optimization of Randomly Textured Surfaces in Thin-Film Solar Cells. *Opt. Express* **2010**, *18*, A335–A342.
29. van Lare, M.; Lenzmann, F.; Verschuuren, M. A.; Polman, A. Mode-Coupling by Plasmonic Surface Scatterers in Thin-Film Si Solar Cells. *Appl. Phys. Lett.* **2012**, *101*, 221110.
30. Yang, J.; You, J.; Chen, C.; Hsu, W.; Tan, H.; Zhang, X.; Hong, Z.; Yang, Y. Plasmonic Polymer Tandem Solar Cell. *ACS Nano* **2011**, *5*, 6210–6217.
31. Wu, J.; Chen, F.; Hsiao, Y.; Chien, F.; Chen, P.; Kuo, C.; Huang, M.; Hsu, C. Surface Plasmonic Effects of Metallic Nanoparticles on the Performance of Polymer Bulk Heterojunction Solar Cells. *ACS Nano* **2011**, *5*, 959–67.
32. Ouyang, Z.; Pillai, S.; Beck, F.; Kunz, O.; Varlamov, S.; Catchpole, K.; Campbell, P.; Green, M. Effective Light Trapping in Polycrystalline Silicon Thin-Film Solar Cells by means of Rear Localized Surface Plasmons. *Appl. Phys. Lett.* **2010**, *96*, 261109.
33. Andreani, L.; Kowalczewski, P.; Mura, C.; Patrini, M.; Acciarri, M.; Binetti, S.; Sassella, A.; Marchionna, S. Towards CIGS Solar Cells with Reduced Film Thickness: A Study of Optical Properties and of Photonic Structures for Light Trapping. 27th European Photovoltaic Solar Energy Conference and Exhibition; **2012**.
34. Schmid, M.; Klenk, R.; Lux-Steiner, M. C.; Topič, M.; Krč, J. Modeling Plasmonic Scattering combined with Thin-Film Optics. *Nanotechnology* **2011**, *22*, 025204.
35. Schmid, M.; Klaer, J.; Klenk, R.; Topič, M.; Krč, J. Stability of Plasmonic Metal Nanoparticles Integrated in the Back Contact of Ultra-Thin Cu(In,Ga)S_2 Solar Cells. *Thin Solid Films* **2013**, *527*, 308.
36. Colin, C.; Massiot, I.; Cattoni, A.; Vandamme, N.; Dupuis, C. Broadband Light-Trapping in Ultra-Thin Nano-Structured Solar Cells. Proc. SPIE 8620, **2013**.
37. Orgassa, K.; Schock, H. W.; Werner, J. H. Alternative Back Contact Materials for Thin Film Cu(In,Ga)Se_2 Solar Cells. *Thin Solid Films* **2003**, *431−432*, 387–391.
38. Brémaud, D. J. L. Investigation and Development of CIGS Solar Cells on Flexible Substrates and with Alternative Electrical Back Contacts. Ph.D. thesis, ETH Zurich, 2009.
39. Verschuuren, M. A. Substrate Conformal Imprint Lithography for Nanophotonic. Ph.D. thesis, Utrecht University, 2010.
40. Ahn, S.; Guo, L. Large-Area Roll-to-Roll and Roll-to-Plate Nanoimprint Lithography: A Step toward High-Throughput Application of Continuous Nanoimprinting. *ACS Nano* **2009**, *3*, 2304–2310.
41. Lumerical FDTD Solutions. https://www.lumerical.com/tcad-products/fdtd/.
42. Ferry, V. E.; Verschuuren, M. A.; Lare, M. V.; Schropp, R. E. I.; Atwater, H. A.; Polman, A. Optimized Spatial Correlations for Broadband Light Trapping Nanopatterns in High Efficiency Ultrathin Film a-Si:H Solar Cells. *Nano Lett.* **2011**, *11*, 4239–4245.
43. Vermang, B.; Wätjen, J.; Fjällström, V.; Rostvall, F.; Edoff, M.; Kotipalli, R.; Henry, F.; Flandre, D. Employing Si Solar Cell Technology to Increase Efficiency of Ultra-Thin Cu(In,Ga)Se_2 Solar Cells. *Prog. Photovoltaics* **2014**, *22*, 1023–1029.
44. Chirila, A.; Reinhard, P.; Pianezzi, F.; Bloesch, P.; Uhl, A. R.; Fella, C.; Kranz, L.; Keller, D.; Gretener, C.; Hagendorfer, H.; *et al*. Potassium-Induced Surface Modification of

Cu(In,Ga)Se_2 Thin Films for High-Efficiency Solar Cells. *Nat. Mater.* **2013**, *12*, 1107–1111.
45. Jackson, P.; Hariskos, D.; Wuerz, R.; Kiowski, O.; Bauer, A.; Powalla, M.; Friedlmeier, T. M. Properties of Cu(In,Ga)Se2 Solar Cells with New Record Efficiencies up to 21.7%. *Phys. Status Solidi RRL* **2015**, *9*, 28–31.
46. Yin, G. Preparation of Ultra-thin $CuIn_{1-x}Ga_xSe_2$ Solar Cells and Their Light Absorption Enhancement. Ph.D. thesis, Technical University Berlin, 2015.
47. Witte, W.; Spiering, S.; Hariskos, D. Substitution of the CdS Buffer Layer in CIGS Thin-Film Solar Cells; Status of Current Research and Record Cell Efficiencies. *Vak. Forsch. Prax.* **2014**, *26*, 23–27.
48. Palik, E.; Ghosh, G. *Handbook of Optical Constants of Solids*; Academic Press: New York, Vol. 3, 1997.
49. Schmid, M.; Krč, J.; Klenk, R.; Topič, M.; Lux-Steiner, M. Optical Modeling of Chalcopyrite-Based Tandems considering Realistic Layer Properties. *Appl. Phys. Lett.* **2009**, *94*, 053507.
50. Schmid, M.; Caballero, R.; Klenk, R.; Krč, J.; Rissom, T.; Topič, M.; Lux-Steiner, M. Experimental Verification of Optically Optimized $CuGaSe_2$ Top Cell for Improving Chalcopyrite Tandems. *EPJ Photovoltaics* **2010**, *1*, 10601–10603.
51. Gabor, A. M.; Tuttle, J. R.; Albin, D. S.; Contreras, M. A.; Noufi, R.; Hermann, A. M. High-Efficiency $CuIn_xGa_{1-x}Se_2$ Solar-Cells Made from $(In_xGa_{1-x})_2Se_3$ Precursor Films. *Appl. Phys. Lett.* **1994**, *65*, 198–200.
52. Kaufmann, C.; Caballero, R.; Unold, T.; Mönig, H.; Hesse, R.; Klenk, R.; Schock, H. Low Temperature Growth of Cu(In,Ga)Se_2. 23th European Photovoltaic Solar Energy Conference and Exhibition; **2008**.